1 **Title**
2 **Path integration impairments reveal early cognitive changes in Subjective Cognitive**
3 **Decline**
4 Short title: Path integration in Subjective Cognitive Decline
5
6 **Authors**
7 Vladislava Segen[1]*, Md Rysul Kabir[2], Adam Streck[3], Jakub Slavik[4], Wenzel Glanz[1,5],
8 Michaela Butryn[1,5], Ehren Newman[6], Zoran Tiganj[2,6], Thomas Wolbers[1,7]
9
10 **Affiliations**

11 1 Aging, Cognition & Technology Group, German Center for Neurodegenerative Diseases
12 (DZNE), Magdeburg 39120, Germany

13 2 Department of Computer Science, Indiana University, Bloomington, USA

14 3 Institute for Computational Cancer Biology (ICCB), Center for Integrated Oncology (CIO),
15 Cancer Research Center Cologne Essen (CCCE), Faculty of Medicine and University Hospital
16 Cologne, University of Cologne, Germany

17 4 The Czech Academy of Sciences, Institute of Information Theory and Automation, Prague,
18 Czech Republic

19 5 Institute for Cognitive Neurology and Dementia Research, Otto-von-Guericke University,
20 Magdeburg, Germany

21 6 Department of Psychological and Brain Sciences, Indiana University, Bloomington, USA

22 7 Center for Behavioural Brain Sciences (CBBS), Otto-von-Guericke-University Magdeburg,
23 Magdeburg 39120, Germany

24 * Corresponding author: Vladislava Segen: Vladislava.Segen@dzne.de

25 † Equal senior authors

26 **Abstract**
27 Path integration, the ability to track one's position using self-motion cues, is critically
28 dependent on the grid cell network in the entorhinal cortex, a region vulnerable to early
29 Alzheimer's disease pathology. In this study, we examined path integration performance in
30 individuals with subjective cognitive decline (SCD), a group at increased risk for Alzheimer's
31 disease, and healthy controls using an immersive virtual reality task. We developed a Bayesian
32 computational model to decompose path integration errors into distinct components. SCD
33 participants exhibited significantly higher path integration error, primarily driven by increased
34 memory leak, while other modelling-derived error sources, such as velocity gain, sensory and
35 reporting noise, remained comparable across groups. Our findings suggest that path integration
36 deficits, specifically memory leak, may serve as an early marker of neurodegeneration in SCD
37 and highlight the potential of self-motion-based navigation tasks for detecting pre-symptomatic
38 Alzheimer's disease-related cognitive changes.
39

40 **Teaser**
41 Virtual reality, computational modelling, and biomarkers uncover path integration deficits,
42 distinguishing pre-symptomatic Alzheimer's from normal aging.

1

MAIN TEXT

Introduction

Spatial navigation is a multifaceted behaviour involving various cognitive processes such as memory storage and retrieval, multisensory integration, and decision-making. Central to navigation is path integration (PI), a process of continuously updating one's position and orientation based on the integration of self-motion cues[1]. This mechanism is crucial for the development of cognitive maps, aiding in the association of environmental cues with location estimates[2]. PI is thought to critically depend on grid cell computations in the entorhinal cortex (EC)[3], which is also the first neocortical region to exhibit tau pathology and neurodegeneration in Alzheimer's disease (AD)[4]. Consistent with these findings, impaired grid cell dynamics and navigation deficits are evident early in AD mouse models[5, 6]. In humans, young APOE-e4 carriers, a known risk factor for AD, have shown altered grid-like BOLD signals[7]. Moreover, behavioural work has suggested corrupted PI in patients with Mild Cognitive Impairment (MCI) and early AD[8, 9], particularly in cases when AD-related pathology is present. Howett et al. (2019) even demonstrated that (i) PI performance was more sensitive at discriminating between AD biomarker positive vs. negative MCI patients compared to standard neuropsychological assessments, and (ii) that PI performance was related to CSF tau and EC volume, further outlining the link between PI and AD-related pathology.

Despite the evidence that PI is affected in MCI and early AD, it remains unknown whether PI deficits emerge at earlier stages of the disease, before traditional cognitive symptoms become apparent. Earlier identification is particularly important as it opens a window for potential interventions at a stage when treatment could be more effective, potentially altering the disease trajectory[10, 11]. Subjective Cognitive Decline (SCD) presents a unique opportunity in this regard, because it is increasingly acknowledged as potentially the earliest stage of AD[12]. Older adults with SCD self-report cognitive deficits that are not detectable through standard neuropsychological testing[13], and they have shown signs of tau pathology in EC [14]. To date, however, it is unknown if PI is affected in SCD and, if so, what mechanisms may represent the earliest degradation of PI due to emerging AD pathology.

To achieve a nuanced understanding of the mechanisms that could underlie PI impairments in SCD, we developed a hierarchical Bayesian model that decomposes observed PI errors into distinct components. Our model builds upon previous leaky integrator models[15–17] that assume a linear accumulation of errors with time or distance, influenced by the leaking of information from the memory trace. Parameters of the model include memory 'leak', velocity gain, additive bias, accumulating noise and reporting noise. By incorporating these parameters, the model accounts for noise, representing random fluctuations, and biases, indicating systematic deviations from the true path, both of which contribute to the overall accuracy of the PI process. Unlike previous models that were based on maximum likelihood, which yield point estimates of parameters, the Bayesian approach estimates full posterior distributions[18], allowing for a richer quantification of uncertainty. Additionally, its hierarchical structure enables the simultaneous modelling of individual differences and group-level effects, offering deeper insights into the variability of PI impairments in SCD. By incorporating prior information, the Bayesian framework is also more robust to noisy data.

To determine if and how PI is impaired in preclinical AD, we tested patients with SCD and matched controls on an immersive, self-guided virtual reality-based PI task. We eliminated distal cues and utilised curved paths to more accurately replicate continuous PI observed in animal studies, minimising reliance on non-spatial heuristics and configural strategies

2

commonly associated with triangular paths in human experiments(*19–21*). Additionally, given the reports that early AD may be associated with angular deficits(*22*) we complemented our PI task by including a novel response to assess angular integration, without being confounded by distance encoding as in previous studies (e.g.(*22, 23*), see (*19*) for further discussion). To preview, our results show that individuals with SCD exhibit larger PI errors compared to controls, driven by increased memory leak as revealed by computational modelling. Importantly, these deficits were not associated with differences in angular integration, movement dynamics, or visual distance estimation, underscoring the specificity of PI impairments in SCD.

Results

Data were collected from 102 participants, comprising 72 controls and 30 individuals with SCD. No significant differences were observed between the groups in terms of neuropsychological assessments, self-reported navigation abilities, and visuo-spatial working memory (Table 1). The SCD group was slightly older ($BF_{10} = 1.916$), and controls performed slightly better on the gait assessment ($BF_{10} = 3.057$), although both groups scored near ceiling (12-point maximum).
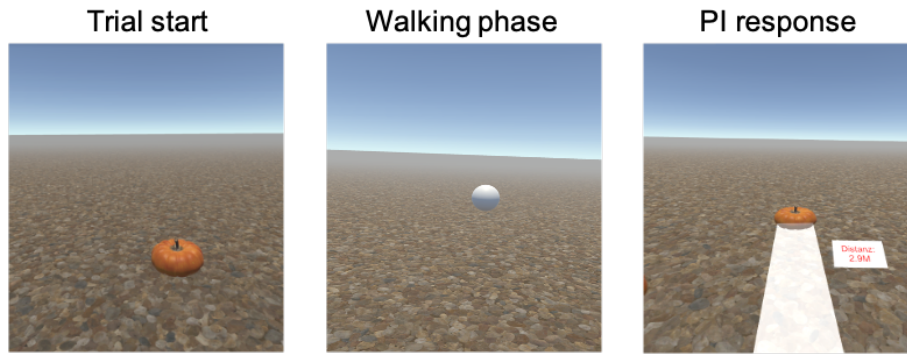
To measure PI, participants engaged with an immersive virtual reality environment through a head-mounted display. They navigated the environment using self-motion cues (vestibular, proprioceptive, motor efference copies and optic flow). For the PI task (Fig. 1), participants followed a floating object along eight distinct pre-defined curved paths (Fig. S1). They were required to report two key metrics at designated stopping points (Stop 1 and Stop 2, Fig. 1): 1) initial heading orientation (angular integration [AI] response), and 2) distance and direction back to the start of the path (PI response). Some trials featured only a single stopping point at the end of the path (Fig. 1; see Methods). After outlier exclusion, both groups presented a comparable number of valid trials for analysis (Table 1).
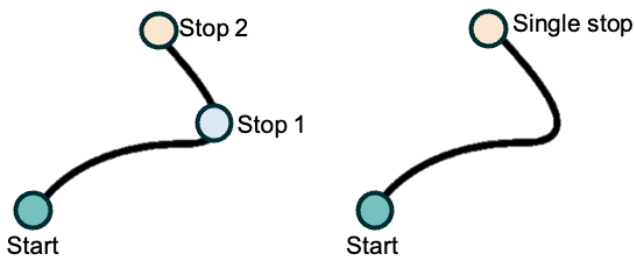
Table 1 Demographic characteristics

|	Control Mean (*SD*)	SCD Mean (*SD*)	**BF10**
Age	65.5 (*5.68*)	68.7 (*7.76*)	**1.916**
MoCA	27.0 (*1.80*)	26.7 (2.00)	0.274
Self-reported spatial abilities	69.4 (*22.80*)	78.5 (*24.8*)	0.868
Visuo-spatial working memory (corsi block task)	4.5 (*0.96*)	4.58 (*0.898*)	0.236
Gait (subset of functional gait assessment task(*24*)	11.3 (*1.01*)	10.6 (*1.40*)	**3.057**
Completed PI trials	80.5 (*14.90*)	78.8 (*19.0*)	0.252
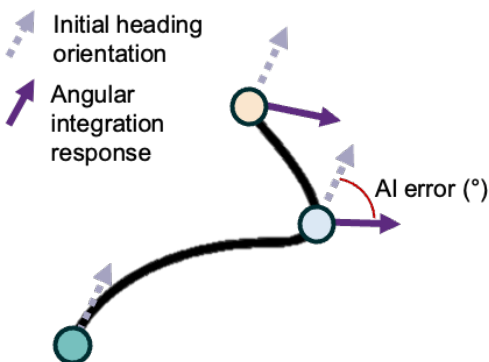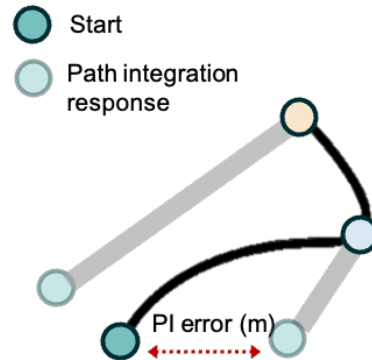
Fig. 1. Task Schematic for Path Integration and Angular Integration

(Top) **Example of the immersive virtual reality environment illustrating the key stages of the task.** Participants started at a designated point marked by a visible object (e.g., a pumpkin). They then followed a curved path by walking towards a floating white sphere (object no longer visible). At the stopping point, they performed the path integration response by repositioning the object to its original location. This was done by turning and estimating the distance using a white line displayed on the ground within the virtual environment. Participants also saw a numerical representation of the response line length, which allowed them to fine-tune their distance estimates by comparing visual and numerical cues. Participants also performed an angular integration response (not shown), by rotating to what they thought is their initial heading orientation (see bottom panel). An example video is available in supplementary materials. (Middle) **Example of a curved path**, performed either with two stopping points, Stop 1 in the middle of the path and Stop 2 at the end (left), or with a single stop at the end of the path (right). (Bottom) **Representation of key task elements and metrics**. (Left) Participants angular integration (AI) response example, where participants are asked to indicate their initial heading orientation at each stopping point by rotating their head and body. Dashed line represents the initial heading orientation and solid purple line represents the AI response. The absolute difference between the two represents AI error. (Right) For the path integration

4

1   (PI) response, participants were asked to indicate the start position of the path by turning to the
2   "presumed" start location and then indicating distance to start. The difference between the start
3   location and the PI response indicates path integration error (m). Participants perform both
4   responses (angular and path integration) at each stopping point.
5
6   **SCD patients show reduced PI performance**
7   Using a regression model, for group and stopping point with age, sex and MoCA scores as
8   covariates, we found that participants with SCD exhibited larger PI errors compared to healthy
9   controls (Estimate =0.257, SE = 0.065, t =3.925, p<0.001, Fig. 2a). Both groups demonstrated
10 higher PI error at the 2nd stopping point at the end of the path relative to the intermediate
11 response points (Estimate = 0.560, SE = 0.090, t = 6.245, p<0.001, Fig. 2b). Critically, there
12 were no significant differences in PI errors for the final stop between trials with or without
13 intermediate stopping points for either group (t=1.238, p=0.217), suggesting that in both
14 groups, errors increased with increasing walked distance from the start location. Replicating
15 previous findings, PI errors increased with advancing age (Estimate = 0.427, SE = 0.063, t =
16 6.728, p<0.001, Fig. 2d), and females exhibited higher PI errors than males (Estimate = 0.306,
17 SE = 0.067, t = 4.557, p<0.001, Fig. 2c). Full regression results are reported in supplementary
18 materials (Table S1). We assessed whether participants performed better than chance on the PI
19 task. Both groups outperformed chance at the first stopping point. However, at the final
20 stopping point, SCD participants did not perform above chance, while controls maintained
21 above-chance performance in trials without an intermediate stopping point (Fig. S2).
22
23
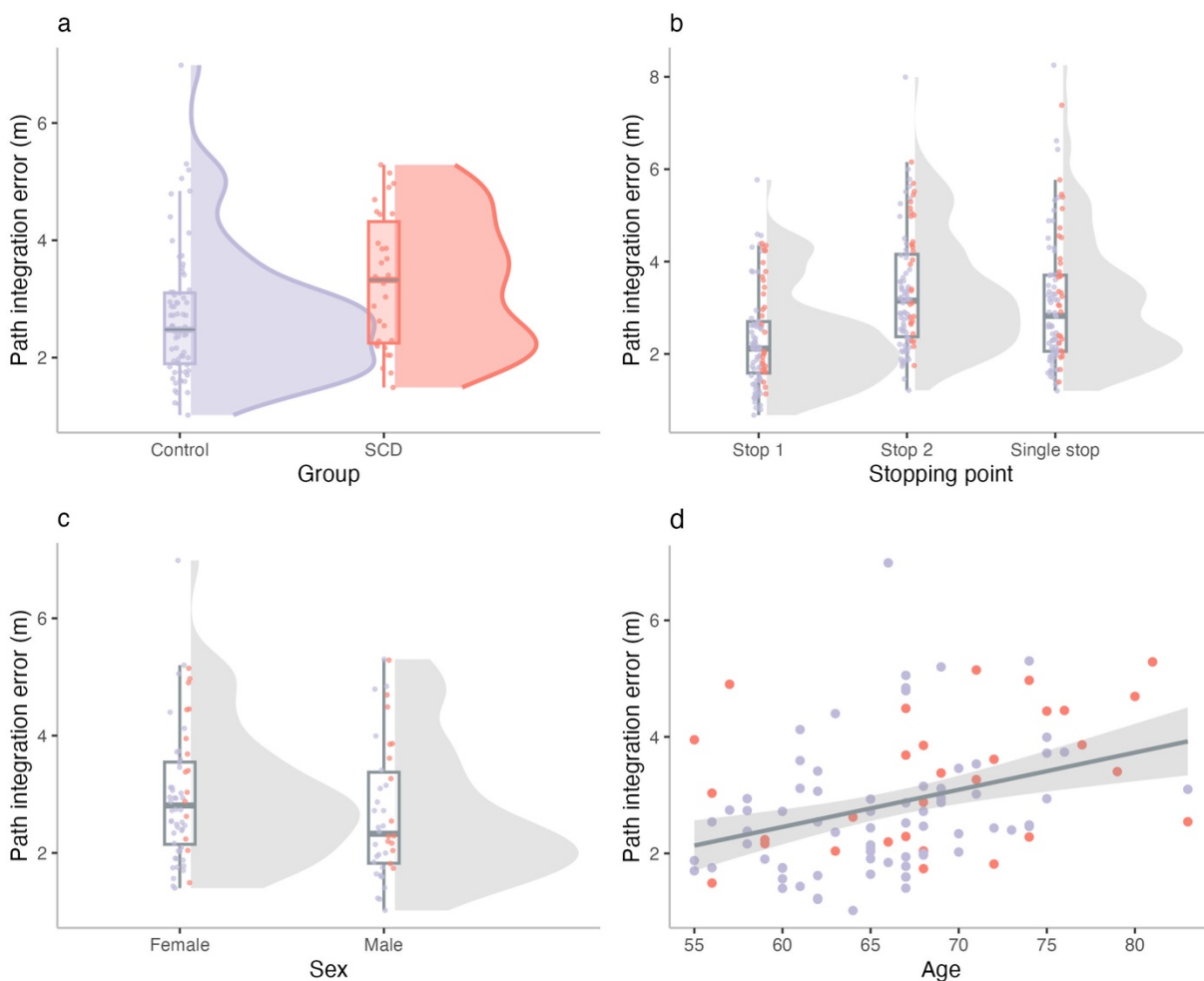
24

1 **Fig. 2. Path integration performance**. a) Group differences in PI error; healthy controls
2 exhibited significantly lower PI errors compared to the SCD group, b) with errors increasing at
3 the final stopping point relative to intermediate points in both groups. c) Sex differences in PI
4 error; females exhibited significantly higher PI errors compared males. d) PI error increased as
5 a function of age across both groups.
6
7 In contrast to PI error, there were no differences in AI error between the groups (BF_{10} =0.285,
8 Fig. 3a), with both groups performing significantly better than chance (Control: mean= 50.92°,
9 BF_{10} = 46.457; SCD: mean= 54.49°, BF_{10} = 15.583). Similar to PI error, we found higher AI
10 error between the 2nd stopping point at the end of the path relative to the intermediate response
11 points (Estimate = 12.565°, SE = 1.859, t = 6.758, p<0.001, Fig. 3b). We also found that AI
12 error was lower for the final stop without an intermediate stopping point, compared to the final
13 stop preceded by an intermediate stopping point (Estimate = -3.720, SE = 1.859, t = -2.001,
14 p=0.046, Fig. 3b). Finally, AI error was associated with increasing age and was higher in
15 females compared to males (Table S2).
16
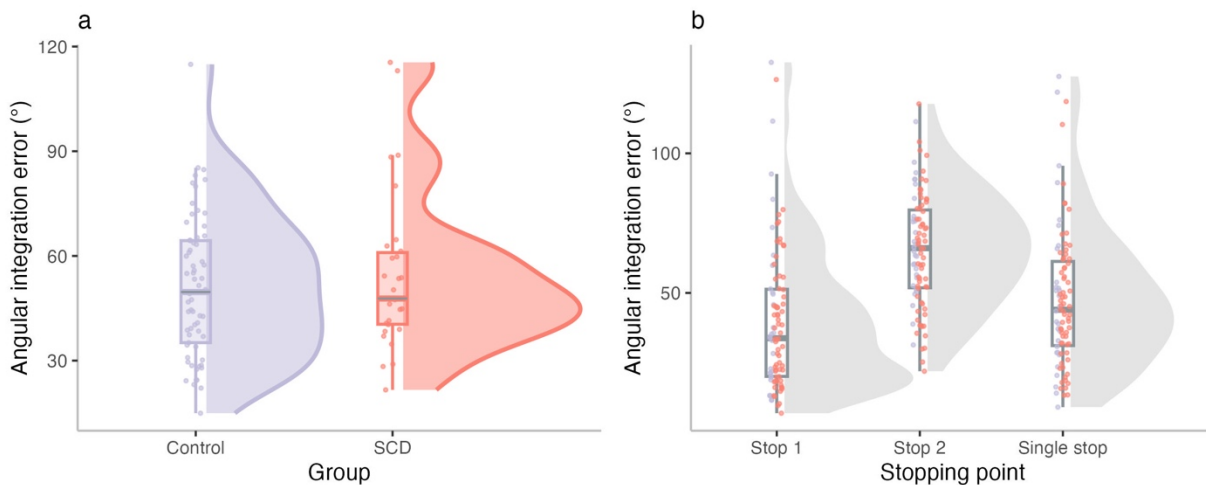
17
18 **Fig. 3. Angular integration performance.** a) Group differences in AI error between groups;
19 no differences in angular integration (°) error between Control and SCD groups. b) AI error
20 across stopping points; higher angular integration error for Stop 2 vs Stop 1, and lower angular
21 integration error at the end of the path in trials with only a single stop compared to trials with
22 an intermediary stop point.
23
24 **Movement characteristics and visual distance perception are unlikely to drive PI**
25 **differences between groups**
26 To test whether group differences in PI error were driven by movement dynamics, we
27 compared head movements, angular and translational velocity, and head pitch (Fig. S3) using
28 Bayesian t-tests, assessing evidence for the null hypothesis. Controls and SCD neither differed
29 in head movements during walking, (BF_{01}=4.193) nor in translational (BF_{01}=4.167) and angular
30 velocities (BF_{01}=2.031).
31 We further examined whether SCD participants sampled the environment differently by
32 looking downward more frequently during walking, which could impair optic flow
33 perception(*25, 26*). Since gaze behaviour was not recorded, head pitch data from the HMD
34 served as a proxy, revealing no group differences (BF_{01}=2.066). Together, with all analyses
35 yielding BF_{01} >1, we conclude that movement dynamics are unlikely to contribute to the
36 differences in PI error between groups.
37

1   Next, we examined changes in PI performance and movement dynamics from early to late
2   trials (comparing the first 10% vs. last 10% of trials; Fig. S4) to ensure no differences in
3   learning dynamics or task adaptation between groups, which could confound PI performance
4   interpretations. First, we did not find any changes in PI performance between early and late
5   trials (estimate = -0.021, SE = 0.094, t = -0.228, p = 0.820), with no significant interaction
6   between group and trial stage (estimate =-0.076, SE = 0.094, t = -0.814, p = 0.416). In terms of
7   movement dynamics, we observed an increase in translational and angular velocity between
8   early and late trials (Translation: estimate = 0.026, SE = 0.003, t = 10.257, p < 0.001; Angular:
9   estimate = 1.814, SE = 0.243, t = 7.467, p < 0.001), with similar patterns for path groups
10   (Translation: p=0.864; Angular: p= 0.983). Additionally, both groups showed an overall
11   decrease in head movements in later trials (estimate = -100.879, SE = 14.934, t = -6.755, p <
12   0.001), potentially reflecting that participants realised the futility of extensive head movements
13   due to the lack of distal cues in the environment, with no interaction between group and trial
14   stage (p=0.297). Finally, head pitch remained unchanged across trials (p= 0.804), with no
15   group or trial stage interactions (p=0.615).
16
17   In addition to the PI task, we included a distance estimation task to assess potential differences
18   in visual distance perception and response precision between control and SCD participants.
19   Participants memorised and reproduced distances to an object (1.4, 3.4, and 5.9 metres) using a
20   virtual ruler. We found no significant group differences in distance estimation (estimate =
21   0.018, SE = 0.011, t = 1.635, p = 0.103, Fig. S5), suggesting comparable visual distance
22   perception and estimation across groups. Both groups exhibited a Weber's law-like effect, with
23   error increasing as the distance increased from 1.4 to 3.4 metres (estimate = 0.202, SE = 0.015,
24   t = 13.340, p < 0.001) and further from 3.4 to 5.9 metres (estimate = 0.155, SE = 0.015, t =
25   10.259, p < 0.001). Additionally, distance error increased with increasing age (estimate =
26   0.005, SE = 0.002, t = 3.314, p < 0.001).

27   **Characterising error sources with a computational model**

28   To better understand the mechanisms that contribute to the observed PI errors, we developed
29   an extended computational model based on the distance-based framework introduced by Stangl
30   et al.(*17*). This enhanced model addresses gaps in prior approaches by capturing both
31   individual variability and shared characteristics of healthy aging and early pathological
32   changes (i.e., SCD). Our model simulates participants' internal location estimates during PI
33   using a two-dimensional diffusion equation, incorporating memory leak (β), velocity gain (α),
34   additive bias (**b**) and accumulating noise (σ_0). Internal estimates are generated based on
35   reported distance ($\hat{d}$) and angle, with addition of Weber-like reporting noise (σ_r) drawn from a
36   normal distribution with zero mean and standard deviation proportional to the reported distance
37   ($\hat{d}$).

38   To infer the model parameters (β, α, **b**, σ_0, σ_r), we utilized a Bayesian hierarchical approach,
39   which provides distinct advantages over traditional methods based on likelihood maximization.
40   Specifically, this approach accounts for individual variability while capturing shared group-
41   level characteristics. The Bayesian framework allows for prior knowledge integration and
42   robust parameter estimation via posterior distributions. Parameter inference was conducted
43   using Markov Chain Monte Carlo (MCMC) sampling with the No-U-Turn Sampler (NUTS),
44   ensuring efficient exploration of the parameter space and reliable posterior estimates(*27*). This
45   model effectively captures variability across individuals and groups, enhancing our
46   understanding of cognitive changes in aging and SCD.

47   **Model selection/evaluation**

1   To determine the most parsimonious model, we compared candidate models combining various
2   error sources (Fig. 4). Model complexity and fit were assessed using expected log predictive
3   density for leave-one-out cross-validation ($elpd_{loo}$)(*28*). The full model showed the best fit,
4   leading us to retain all parameters to explain PI error sources.
5
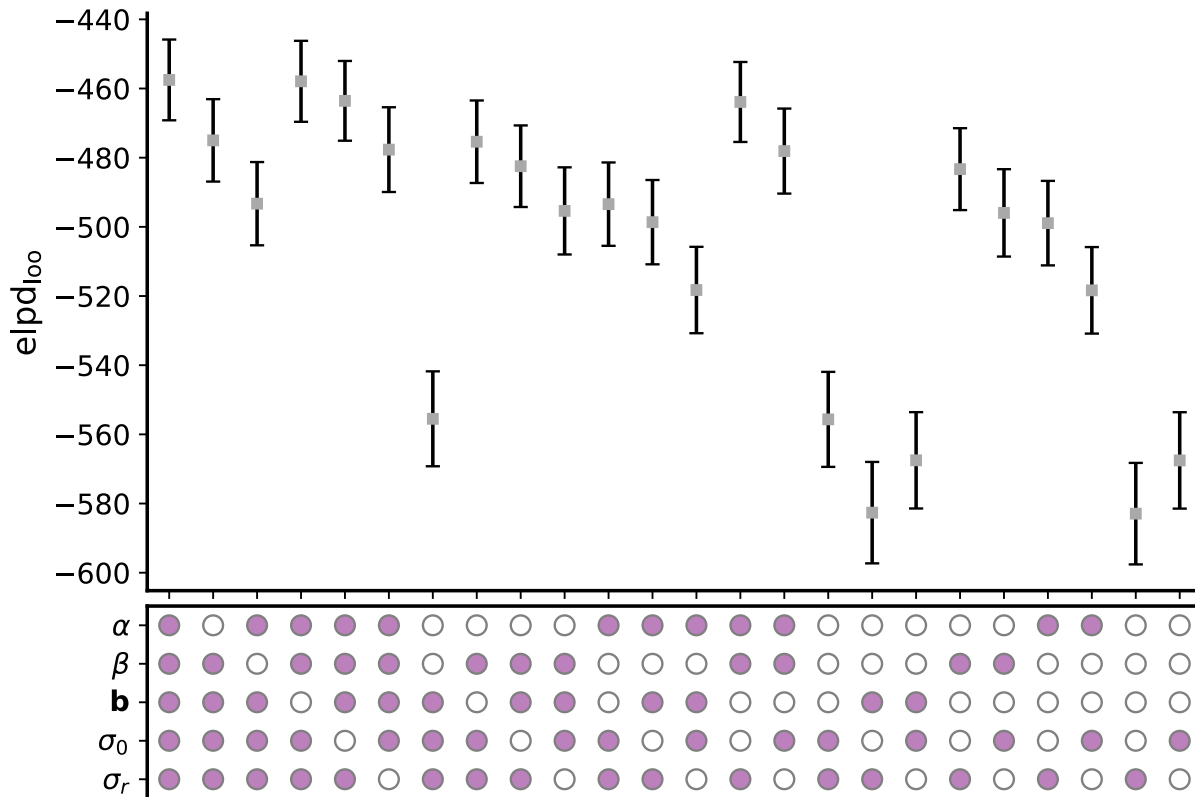
6
7   **Fig. 4. Comparison of Candidate Models Across Error Sources**
8   Comparison of candidate models incorporating different combinations of error sources:
9   velocity gain (α), memory leak (β), additive bias (**b**), accumulating noise (σ_0), and reporting
10 noise (σ_r). Error sources included in each model are represented below the graph as filled
11 (purple). The expected log pointwise predictive density for leave-one-out cross-validation
12 ($elpd_{loo}$) is shown for each model (mean ± SEM). Models with higher $elpd_{loo}$ values indicate
13 better predictive performance. The "full" model demonstrates the best fit to the data (highest
14 $elpd_{loo}$ value).
15
16 **Memory leak distinguishes SCD patients from healthy controls**
17 What are the mechanisms that may have caused increased PI errors in individuals with SCD?
18 To address this question, we first calculated mean parameter estimates for each participant and
19 compared them using linear regression with age and group as covariates (results reported in
20 Table S4). We found that SCD participants exhibited significantly higher memory leak than
21 Controls (β; estimate = 0.055, SE = 0.020, t=2.720, p=0.008, Fig. 5b), indicating a greater
22 tendency for stored information to decay over travelled distance. In contrast, there was no
23 evidence of a significant group difference in velocity gain (α; estimate = -0.025, SE = 0.052, t
24 = -0.493, p = 0.623, Fig. 5a), additive bias ($\|\mathbf{b}\|$; estimate = 0.0001, SE = 0.003, t = 0.044, p =
25 0.965, Fig. 5c), accumulating noise (σ_o^2; estimate = 0.022, SE = 0.025, t = 0.858, p = 0.393,
26 Fig. 5d) and reporting noise (σ_r^2; estimate = 0.031, SE = 0.017, t = 1.820, p = 0.072, Fig. 5e).
27 Across both groups, age was associated with increases in memory leak (β; estimate = 0.008, SE
28 = 0.003, t = 2.720, p = 0.008, Fig. S6a) and reporting noise (σ_r^2; estimate = 0.008, SE = 0.002, t
29 = 3.581, p = 0.001, Fig. S6b).

8

To further assess the robustness of our findings, we examined group differences in PI error sources using the Highest Density Intervals (HDIs) of the posterior distributions of the group-level mean model parameters (see Fig. S7). HDIs provide a comprehensive summary of parameter differences by capturing the most credible range rather than relying solely on point estimates, offering a clearer representation of uncertainty and group differences. HDIs provide a more comprehensive summary of the distribution by highlighting the most credible range of parameter differences rather than relying solely on point estimates. This approach offers a clearer representation of uncertainty and group differences. Consistent with the individual-level analysis, the differences in the posterior distributions of γ for memory leak (β) provide strong evidence for higher values in individuals with SCD compared to controls, with 99.7% of the distribution above zero. In addition, the 95% HDI [0.10,0.76] did not include zero, suggesting a statistically credible and significant group difference. The differences in posterior distributions of the remaining group-level parameters—velocity gain (γ_α), additive bias (γ_b), accumulating noise ($\gamma_{\sigma_0^2}$) and reporting noise ($\gamma_{\sigma_r^2}$) (Fig. 5a, 5c-5e)—exhibited negligible evidence for group differences as their 95% HDIs all overlapped zero. A subsequent ROPE analysis ([-0.1, 0.1]) supported practical equivalence for the remaining parameters, as most of the 95% HDI samples fell within these bounds(29). Together, these findings suggest that SCD is associated with increased memory leak, even after accounting for possible age effects, while other parameters remained comparable between groups across both individual and group-level comparisons.
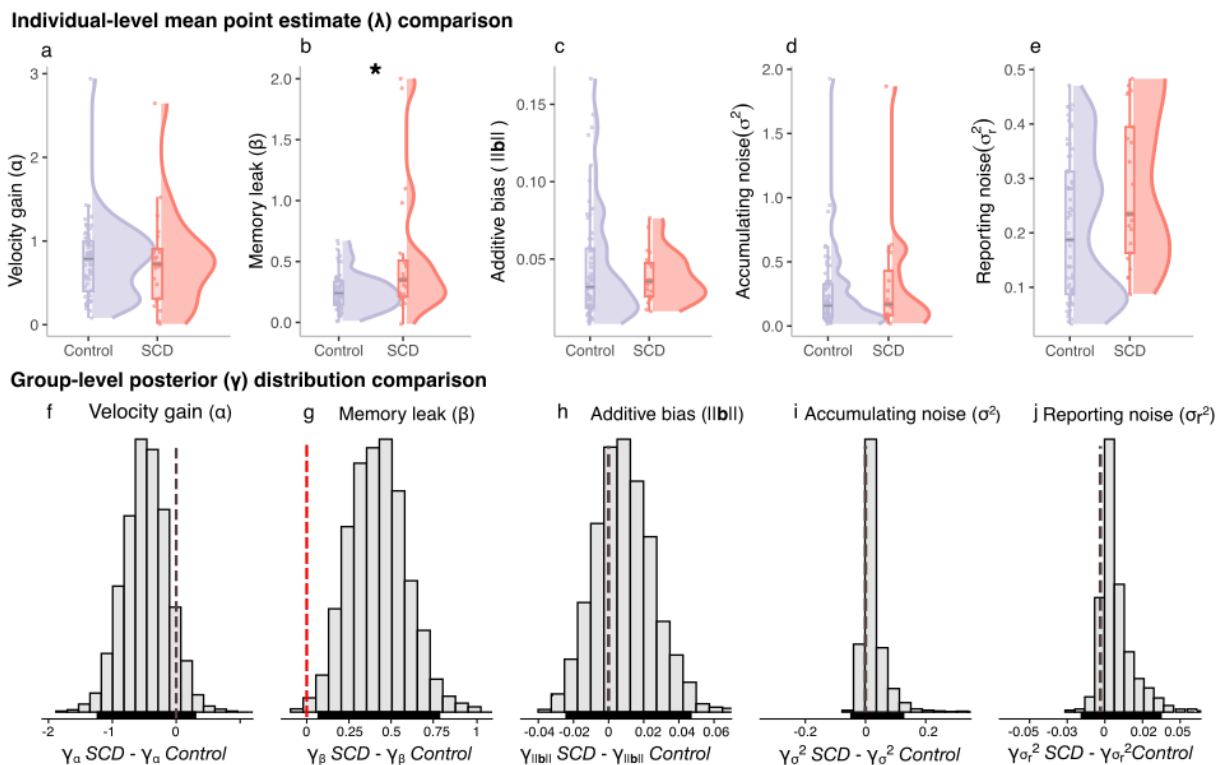
Fig. 5. Comparison of Computational Model Parameters Between Control and SCD Groups Upper panel (a-e) Violin plots showing distributions of individual level mean point estimate comparisons between control and SCD groups for velocity gain (α), memory leak (β), additive bias (||**b**||), accumulating noise (σ_0^2), and reporting noise (σ_r^2) for Control (blue) and SCD (red) participants. SCD participants exhibited significantly higher memory leak (β)

9

1 compared to Controls (g), while other parameters (α, $||\mathbf{b}||$, σ_0^2, and σ_r^2) showed no significant
2 group differences. Asterisk indicates significant effect. Lower panel (f-j) Posterior
3 distributions of the differences between control and SCD groups for the group-level mean
4 parameter γ. The horizontal bars near the x-axis denote the 95% Highest Density Interval
5 (HDI) of the posterior distributions for group differences. Dashed vertical lines indicate zero,
6 and the percentages reflect the proportion of the posterior distribution on either side of zero,
7 providing evidence for the likely direction of group differences. The posterior distributions
8 revealed strong evidence for higher memory leak (β) in individuals with SCD compared to
9 Controls (red dashed line), with 99.7% of the distribution above zero and a 95% HDI excluding
10 zero, indicating a statistically credible group difference. In contrast, posterior distributions of γ
11 for the remaining parameters—velocity gain, additive bias, accumulating noise, and reporting
12 noise—showed negligible evidence for group differences, as their 95% HDIs overlapped zero
13 (black dashed line).
14
15 **Blood NFL Predicts PI Errors, Velocity Gain Deviations, and Increased Reporting Noise**
16 We also obtained plasma-based biological biomarker data related to neurodegeneration from a
17 subset of participants (SCD=27, Control=54). Specifically, we measured plasma levels of
18 neurofilament light chain (NFL), a marker of general neurodegeneration[30, 31], and pTau181,
19 associated with AD-related tau accumulation[31, 32]. We also included APOE (ϵ4 carriers and
20 ϵ4 noncarriers), a risk factor for AD[33], in the analysis. Our analysis of these plasma
21 biomarkers showed no significant differences in the concentrations of NFL (BF_{10}=0.461, Fig.
22 6b) as well as no differences in the number of ϵ4 carriers and ϵ4 noncarriers between Control
23 and SCD groups (χ^2p=0.796, Fig. 6c).
24
25 Next, we investigated the predictive relationship between PI error and blood-based biomarkers,
26 with age included as a covariate. NFL was the only significant predictor of increased PI error
27 (Fig. 6d; estimate = 1.195, SE = 0.370, t = 3.232, p =0.002). Subsequently, to understand the
28 potential biological underpinnings driving distinct error sources contributing to impaired PI we
29 examined if these biomarkers predict individual parameter estimates derived from the
30 computational model. We found that higher NFL levels were predictive of greater deviations
31 from the optimal velocity gain (Fig. 6e; absolute deviation from α=1; estimate = 0.121, SE =
32 0.039, t = 3.183, p =0.002), and increased reporting noise (Fig. 6f; estimate = 0.055, SE =
33 0.018, t = 3.009, p = 0.004). No other biomarkers significantly predicted PI error sources.
34 Based on partial R^2 values, NFL contributed more to predicting reporting noise (0.120) than to
35 velocity gain deviation (0.045).
36
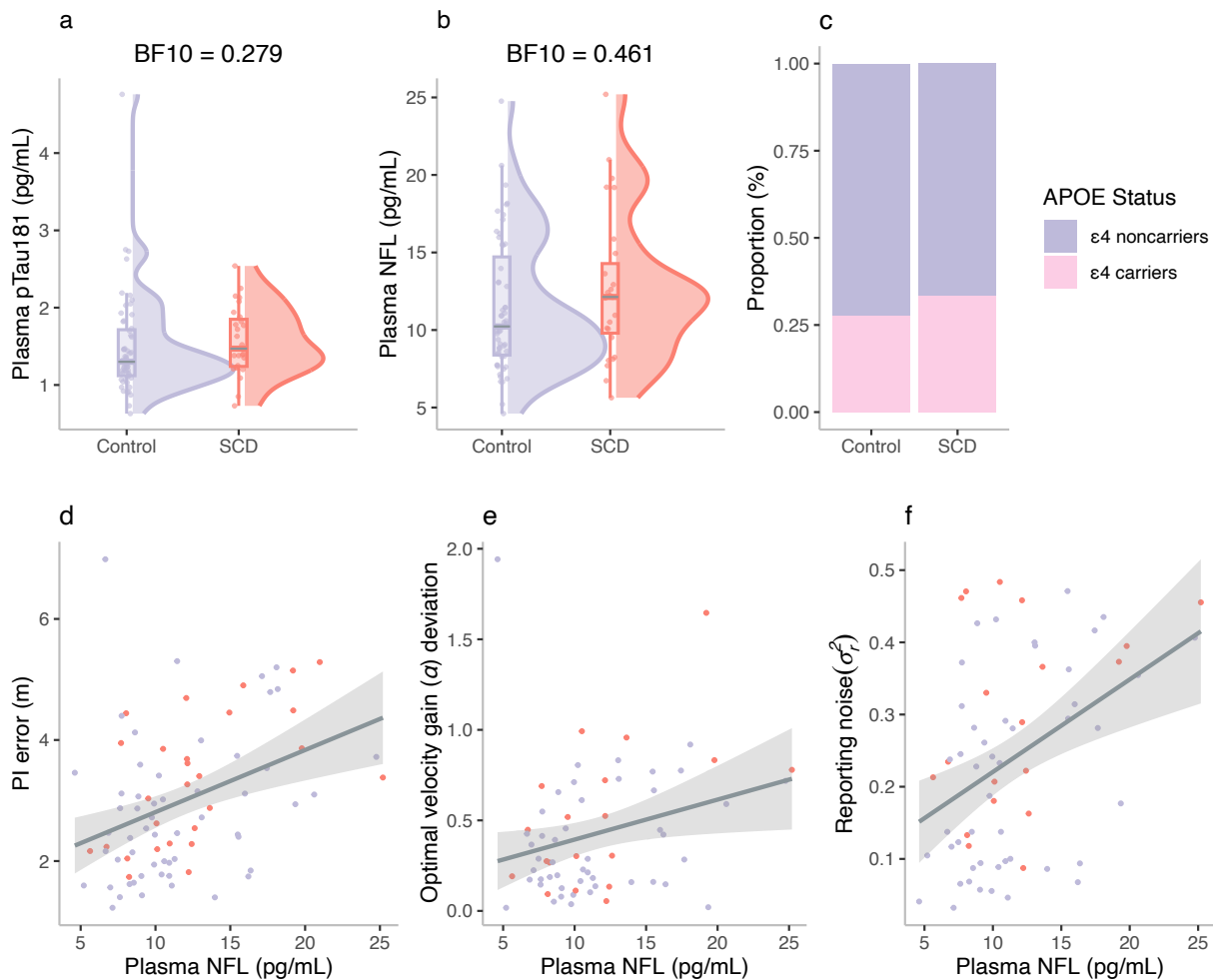
Fig. 6. Plasma Biomarkers, APOE Genotype, and Associations with PI and Error Sources
(a-b) Violin plots showing plasma levels of pTau181 and NFL in Control (blue) and SCD (red) groups. Bayesian analyses provided evidence supporting no group differences in pTau181 (BF_{10} =0.279) and NFL (BF_{10} =0.461). (c) Proportion of APOE ε4 carriers (pink) and noncarriers (blue) across Control and SCD groups, showing no significant differences (p=0.796). (d-f) Scatter plots illustrating the predictive relationship between plasma NFL levels and behavioural outcomes, with age included as a covariate. Higher NFL levels were associated with increased PI error (d), greater deviations from the optimal velocity gain (e), and higher reporting noise (f). Shaded areas represent the 95% confidence interval for regression lines.

Discussion
In this study, we examined PI in individuals with SCD and healthy controls using a self-guided immersive virtual reality task. SCD participants showed significantly higher PI errors than controls. A hierarchical Bayesian model revealed that these deficits were primarily driven by increased memory leak, while other parameters—velocity gain, additive bias, and noise—remained similar between groups. Although no group differences were found in blood biomarkers, NFL, a marker of neurodegeneration, was significantly associated with increased PI errors, velocity gain deviations, and reporting noise.

To the best of our knowledge, this study provides the first evidence for PI impairments in SCD participants, despite their comparable performance to healthy controls on the AI component of the task and in other cognitive domains. Bayesian analyses did not reveal any group differences in head movements, translational and angular velocity, or head pitch, indicating that PI deficits

11

were unlikely to be driven by variations in movement dynamics or sampling strategies, such as a tendency to look downward during navigation. Additionally, both groups exhibited similar changes in performance and movement metrics from early to late trials, with no evidence of group differences in learning or task adaptation. Thereby our results highlight that PI may uniquely tap into subtle changes in neural computations that are difficult to detect with standard cognitive measures, highlighting its potential as a sensitive marker of pre-symptomatic AD.

It is important to note that our experimental design was specifically tailored to reduce potential confounds often seen in PI tasks. By requiring participants to rely primarily on multisensory self-motion cues (vision, proprioception, vestibular and motor efference copies), we minimized the influence of sensory degradation, which is commonly observed with aging and can impair performance when limited sensory modalities are available(*23, 34, 35*). Furthermore, the task excluded proximal and distal landmarks(*7, 9, 36*), reducing the likelihood of compensatory landmark-based navigation or reliance on non-spatial heuristics. These design choices create a more "pure" PI task, where older adults had to continuously update their position in space relying on idiothetic cues. The observed deficits in SCD participants, therefore, likely reflect genuine impairments in PI rather than alternative cognitive or sensory explanations.

To gain a deeper understanding of the mechanisms contributing to the overall PI deficits, we developed a hierarchical Bayesian model that decomposes observed PI errors into distinct components. Critically, we found that **memory leak** was the only parameter that reliably distinguished older adults with SCD from healthy controls. Memory leak, as defined in our model, refers to the gradual decay of the state variable, specifically the homing vector encoding the distance and direction back to the starting point as distance increases during path traversal. Our behavioural findings support that this decay occurs over space rather than time, as indicated by the comparable PI performance at the end of the path in trials with and without intermediate stopping points. Notably, trials without intermediate stops had similar distances but shorter durations, emphasizing that memory leak is more closely tied to movement itself— emerging when positional changes occur—rather than during stationary periods. Thus, we conclude that memory leak is unlikely to be driven by working memory deficits. This interpretation is further supported by the absence of group differences on the Corsi block task, a standard measure of visuo-spatial working memory(*37*).

We propose that these PI deficits are related to impaired grid cell function, which may be - amongst the earliest functional changes during Alzheimer's disease progression(*6, 38, 39*). Grid cells serve as a neural integrator for spatial information supporting PI(*3*), and functional changes in this network may impair the brain's ability to maintain a stable representation of self-location over the course of movement. Animal models of AD show profound loss of grid tuning(*6, 40, 41*) . The additional burden of tau pathology in the EC may disrupt the grid cell network's capacity to prevent "leakage," amplifying memory decay and making it a key distinguishing feature from healthy aging, where some degree of leak may also be present but to a lesser extent (c.f. higher leak with age(*17*)). Indeed, young APOE ε4 carriers exhibit reduced grid-cell-like tuning(*39*) .

While the precise mechanisms as to how AD pathology may lead to greater memory leak remain speculative, we propose several plausible explanations. One possible mechanistic example of how AD pathology could disrupt spatial computations involves altered attractor dynamics within the hippocampal–entorhinal circuit. Grid cell models based on continuous attractor networks create stable spatial maps by maintaining coherent activity patterns representing the organism's location(*42*). In these networks, each new location estimate relies

1 on the previously encoded spatial state and velocity updates. The stability of these attractor
2 networks could be compromised by tau pathology, which effectively reduces the network's
3 "energy well," making attractor states more prone to drift. In such a weakened network, any
4 slight perturbation (e.g., from sensory noise or normal fluctuations in neural firing) can push
5 the representation away from its stable configuration, causing the previously encoded spatial
6 state to degrade more quickly and amplifying PI errors. This instability could be further
7 exacerbated by AD related dysfunction in parvalbumin interneurons, which compromises the
8 inhibitory control needed for precise network dynamics and grid tunning(43, 44). Furthermore,
9 the disruption of axonal transport and synaptic function likely contributes to this weakened
10 network state(45). Consequently, updating spatial position becomes increasingly difficult, with
11 the internal representation eroding faster than under normal conditions.

12 An additional mechanism involves disrupted temporal precision in the sequential updating of
13 the PI signal. Accurate tracking of position relies on rhythmic oscillatory processes—
14 particularly theta and gamma bands—to coordinate neuronal ensembles in the entorhinal-
15 hippocampal circuit(46–52). AD-related changes in the EC may reduce synchrony between
16 grid cells and head-direction cells or attenuate the amplitude of key oscillations, potentially by
17 disrupting the function of interneurons that regulate these rhythms(53, 54). For example,
18 disease related reduction in cholinergic transmission(55) disrupt theta-gamma interactions and
19 grid tunning(56, 57) . Without precisely coordinated neuronal firing, the system struggles to
20 integrate velocity and orientation cues at the correct moments, thereby compounding small
21 discrepancies over successive steps. This disruption of temporal precision could further
22 destabilize the state variable, contributing to the "leak" observed in SCD. Since PI relies on
23 cumulative updates, even minor disruptions in the running position estimate can have a
24 cascading effect, resulting in progressive loss of spatial information manifesting as a gradual
25 "leak" in spatial memory.

26 Contrary to recent findings suggesting pre-clinical or prodromal AD (i.e., MCI, APOE4 status,
27 and other AD-related risks) is associated with higher angular errors(7, 36, 58) with corrupted
28 angular integration as a primary driver of early AD-related deficits(22), we did not observe
29 group differences in AI between healthy older adults and individuals with SCD. Both groups
30 performed significantly better than chance on our AI tasks, despite showing clear differences in
31 PI. This discrepancy may be explained by methodological differences in how AI is assessed.
32 Traditional PI tasks, such as triangle completion, derive distance and angular errors to infer
33 deficits, with distance error as the deviation from the actual start point and angular error as the
34 difference between the correct and reported heading. However, mis-encoding of travelled
35 distance during the outbound path can also induce angular error, potentially confounding the
36 interpretation of angular deficits(19–21). To address this, we incorporated an additional task in
37 which participants were asked to remember and recreate their initial heading orientation at each
38 response point, allowing us to disentangle angular integration from distance encoding and the
39 combined processes required for PI.

40 Our findings of intact AI alongside PI deficits in SCD align with research on AD rodent
41 models. These studies suggest that head direction (HD) cell coding, a critical component for
42 orientation inputs to grid cells(59), is preserved for longer than grid cell integrity during the
43 progression of AD(5, 6). It is possible that impaired AI becomes more prominent at later
44 stages of disease progression, such as aMCI, as supported by recent modelling studies in
45 humans(22). Notably, Ying et al.(5) demonstrated that although HD cells maintain normal
46 firing properties and tuning curves in AD mice, early-stage AD is characterized by reduced
47 synchrony between HD and grid cells. This suggests that impaired integration of orientation
48 and distance information may underlie early PI deficits, as evidenced by intact AI but disrupted

13

PI in SCD, consistent with the interpretation that the EC is responsible for integrating these inputs.

Contrary to previous research(*7, 36, 58*), we did not observe larger PI deficits in APOE ε4 carriers, a known risk factor for sporadic AD, despite employing PI tasks without orientation cues, which are considered highly sensitive to PI impairments in this group (e.g., Colmant et al.,(*58*)). This discrepancy may be partly explained by complex interactions between APOE status, lifestyle factors, and sex, as suggested by prior studies(*36*). Additionally, most research reporting greater PI errors in APOE ε4 carriers has focused on younger populations, such as young adults(*7*) or middle-aged individuals(*36*). In older samples like ours, APOE status may be less informative, with markers such as NFL emerging as stronger predictors of neurodegeneration. One possible explanation is that APOE ε4 carriers predisposed to AD may have already progressed to MCI or dementia, excluding them from our sample. Alternatively, the ε4 carriers in our cohort may represent a subset with protective factors that delay disease progression, as nearly half were cognitively healthy. This aligns with evidence that APOE ε4 expression is modulated by various epigenetic(*60*), environmental and genetic factors(*61*).

Our study found no group differences in blood biomarkers, including NFL and plasma pTau181. This lack of distinction may reflect the nonspecific nature of NFL, which indicates general neurodegeneration rather than AD-specific pathology(*31, 62*). Similarly, while pTau181 is associated with AD, its sensitivity for detecting early or preclinical stages is limited - emerging evidence suggests that other phosphorylated tau isoforms, such as pTau217, may offer greater diagnostic accuracy and specificity for AD-related pathology(*63*). Despite the absence of group differences, NFL predicted PI deficits, with associations observed for higher PI error, velocity gain, and reporting noise. These associations align with NFL's established link to systemic neurodegeneration and white matter pathology(*30, 64*) both critical for efficient neural communication(*65, 66*). Reduced white matter integrity, associated with elevated NFL, may amplify noise across neural networks, contributing to variability in reporting accuracy and PI performance. Furthermore, NFL's link to sensorimotor impairments, such as slower nerve conduction and reduced sensory precision in diabetes(*67*), may further impact motor control and sensory integration, contributing to higher reporting noise. Together, these findings suggest that NFL captures broader neuronal changes that contribute to higher uncertainty and increased variability in response execution across navigation tasks.

In summary, our findings highlight PI deficits as a hallmark of pre-symptomatic AD, with memory leak identified as the key source driving these deficits in individuals with SCD. These results underscore the critical role of grid cell dysfunction in early AD-related PI deficits, likely reflecting the vulnerability of the entorhinal cortex to tau pathology. Our computational model effectively decomposed and distinguished error sources, revealing distinct mechanisms underlying PI deficits in SCD. These findings can inform the design of targeted spatial navigation tasks tailored to detect early AD-related impairments. Moreover, such tasks could provide useful behavioural readouts for clinical trials, enabling a more sensitive evaluation of disease-modifying interventions that aim to mitigate early AD-related cognitive and neural changes.

Materials and Methods
Participants
The study involved 104 participants, divided into two groups. The Control group consisted of 73 individuals (46 females), averaging 65.70 years old (SD = 5.80). The Subjective Cognitive Decline (SCD) group, referred by neurologists from an in-house memory clinic, included 31 participants (15 females), with an average age of 68.45 years (SD = 7.79). SCD classification

was based on a comprehensive clinical interview, including self-reported cognitive concerns and informant feedback, with no objective cognitive impairment detected through neuropsychological testing using the CERAD-plus battery(*68*) . All participants provided informed consent, and the study was approved by the Ethics Committee of the University of Magdeburg. Two subjects (1 SCD and 1 Control) scored below the Montreal Cognitive Assessment (MoCA(*69*) cutoff of 23(*70*) - indicating the presence of mild cognitive impairment - and were hence excluded from further analysis- resulting in the final sample of 102 participants (72 controls and 30 SCD. All subjects had normal or corrected-to-normal vision and were physically capable of standing for extended periods, a prerequisite for completing the PI task. We also obtained self-reported spatial abilities, measured by the 32-item DZNE Questionnaire on Spatial Orientation Skills (DFRO), and visuo-spatial working memory, measured by the Corsi block-tapping task(*37*), implemented using PsyToolkit platform(*71*). In addition to cognitive assessments, participants underwent functional gait analysis using four tasks from the Functional Gait Assessment(*24*), focusing on level surface walking, gait speed variations, narrow base support, and gait with eyes closed. Balance was assessed using eight brief 20-second tasks. However, due to scoring discrepancies among experimenters, these results were not included in the analysis.

Plasma biomarker analysis

Blood samples for pTau181, NFL, NPTX2, and APOE genotyping analysis were obtained from 84 participants. The blood samples were analysed at the clinical research group, Bonn DZNE, using the SIMOA kit, whilst NPTX2 was analysed using the INNOTEST kit from Fujirebio. We did not include NPTX2 in the final analysis because, although it is secreted by neurons and serves as a marker of synaptic integrity(*72*), NPTX2 is also produced in non-neuronal tissues such as the pancreas (pancreatic islets), pituitary gland, and adrenal medulla. This broader expression pattern raises concerns about the specificity of plasma NPTX2 as a reliable marker of synaptic integrity. For APOE genotyping, DNA was extracted from participants' blood samples, analyzed to detect the APOE polymorphisms, and assigned two of the following alleles: ε2, ε3, or ε4. The APOE ε4 allele is a major risk factor of AD(*33*). We classified participants as ε4 carriers (ε3ε4, ε4ε4, and ε2ε4) or ε4 noncarriers (ε2ε2, ε2ε3, and ε3ε3).

Immersive virtual reality path integration task

Participants engaged in a self-guided immersive virtual reality path integration task, performed in a virtual environment featuring an open field devoid of landmarks, with only a ground pebbly texture providing optic flow information. The self-guided nature of the task, where participants chose their preferred walking speed, offered the advantage of minimising experimenter biases and potential dual task costs associated with walking at a predefined speed. This setup also contrasts with other self-guided PI tasks, e.g., the apple game(*7*) or virtual reality-based triangle completion tasks (e.g.,(*9*, *36*)) where external objects act as destination markers to guide participants, potentially enabling them to compute distances using static visual depth perception. This task required them to estimate the distance and direction to their starting point at two different points along each of eight unique sinuous paths - in the middle and at the end. These paths were designed with a variety of left and right turn combinations, ensuring each combination was repeated twice (Fig. S1). Examples include left followed by right turn, right followed by left turn, two consecutive left turns, and two consecutive right turns. The turn sizes varied between 40° and 140°, with the stipulation that the combined turn sizes in the same direction per path did not exceed 180°. This design, devoid of external guiding objects, ensured that distance estimation was based primarily on internal cues rather than visual distance estimation, thus providing a purer assessment of path integration abilities.

15

1

2   The task was developed using Unity software (19.4.0f1) and played through an HTC Vive Pro
3   headset equipped with a wireless setup, enhancing the immersive experience. Each path
4   segment, a portion of the path that contains a single turn in one direction, either leading from
5   the start to the midpoint or from the midpoint to the end, spanned approximately 3 metres,
6   varying with the curvature of the path (beeline distance of 2.7 metres). In about 10% of the
7   trials, participants walked the entire path and provided responses only at the end, resulting in
8   trials of shorter duration but covering the same distance. Each new trial commenced with
9   participants walking towards an object, then facing the start of the path to memorise their
10 position and heading orientation. They then followed a floating sphere to the first stopping
11 point, where they provided both Angular Integration (AI) and Path Integration (PI) responses.
12 After responding, participants were guided to continue the path by following the sphere until
13 reaching the end, where AI and PI responses were again given. The order of AI and PI
14 responses was counterbalanced among participants.

15

16 At each stopping point during the task, participants were asked to orient themselves towards
17 their perceived starting position, using a virtual ruler projected on the ground to indicate the
18 distance to this location. The line's direction was controlled by the participant's head
19 movements, while its length was adjusted using the up and down keys on the HTC Vive
20 controller.

21

22 Besides PI responses, we also obtained an AI response by asking participants to remember and
23 recreate their initial heading orientation at each stopping point, achieved by physically rotating
24 to their perceived initial heading and pressing the trigger on the HTC Vive controller. This
25 additional task, which was based on earlier work[21], aimed to assess participants' ability to
26 integrate heading changes (AI) without the confounding factor of distance integration, differing
27 from standard approaches of decomposing the PI response into distance and angular error (see
28 Segen et al.,[19] for further discussion).

29

30 **Experimental procedure**
31 The study was conducted over two separate days, with sessions lasting three hours each.
32 Participants initially engaged in six practice trials. The main trials were organised into blocks
33 of 14, interspersed with mandatory short breaks. At the end of each block, participants
34 undertook three additional distance estimation trials, requiring them to recall and then replicate
35 specific distances - 1.4, 3.8, and 5.9 meters - using a virtual ruler, without physical movement.
36 This task was included to investigate potential differences in visual distance estimation and
37 response noise between the control and SCD groups.

38

39 A subset of the subjects in the control group performed PI tasks without the AI response, due
40 to technical difficulties, we included these subjects in the analysis, as their PI error was similar
41 to those who provided both the PI and AI responses (Fig. S8).

42

43 **Behavioral data analysis**
44 **Outlier removal**
45 A 2-step outlier removal procedure was applied. First, we removed trials where an accidental
46 response was registered either due to technical issues or participants' use of the controllers.
47 These trials were identified as follows: trials less than 2 seconds (lowest possible time), trials
48 with distance responses less than .4 meters (minimum set distance), trials with identical
49 distance to the random lengths of the line at the beginning of the response (within .01m
50 threshold). We also removed all trials that had response times over 60 seconds (longer response
51 times often accompanied by loss of connection, or interruptions due to clarifications from

subjects about the task). The second step included removal of outliers based on PI task using the interquartile range method on individual path integration error (m) distributions to remove occasional trials where participants might have temporary lost concentration or got disoriented. Overall, this resulted in the exclusion of 4.63% of the data. We repeated a similar outlier removal procedure for the AI responses. Specifically, only responses with response times between 2-60 seconds were included. Next, we used the interquartile range method on individual angular integration error (°) distributions; overall, 6.33% of AI data was removed.

For distance estimation trials, outliers were removed for each participant and each level of distance using the interquartile range method, which resulted in the exclusion of 6.46% of the data

Path integration metric calculation

The x and y coordinates of the presumed starting point according to the participant's response were calculated by:

$$x_{presumed} = x_{stop} + d \cdot cos(ori_{response})$$
$$y_{presumed} = y_{stop} + d \cdot sin(ori_{response})$$

where d is the response distance, and $ori_{response}$ is the responded orientation. x_{origin} and y_{origin} are coordinates of the start point, $x_{presumed}$ and $y_{presumed}$ are the resulting coordinates of the presumed starting point. To determine the path integration error for a given stopping point, the Euclidean distance between the presumed starting point (according to the participant's response at this respective stopping point) and the starting point was calculated

$$PIerror = \sqrt{\left(x_{presumed} - x_{origin}\right)^2 + \left(y_{presumed} - y_{origin}\right)^2}$$

Angular integration metric calculation

Angular integration error was calculated using the absolute difference between the initial heading orientation at the starting point (orientation indicated to participants using an arrow on the floor of the virtual environment) and the angular orientation response at each stopping point.

Modelling analysis
Outlier removal

To model error sources, an additional outlier removal criterion was applied, excluding subjects with fewer than 50 valid PI trials after data pre-processing. This resulted in the removal of 8 subjects (5 controls and 3 SCD). Following parameter estimation, we further excluded subjects with negative velocity gain (α). This led to the exclusion of an additional 10 participants (6 SCD and 4 controls). Examination of individual responses in this group revealed a common tendency to "fail" to turn during their PI response, contributing to the negative velocity gain. A detailed analysis of the error patterns and response profiles of these participants is provided in the supplementary materials.

Given that these 18 participants were excluded from the modelling analysis, we conducted a re-analysis of the behavioural data, also excluding these individuals, and present the results in the supplementary materials for comparison.

Internal estimate model

We used the distance model from Stangl et al.(*17*) where internal location estimates of the participants' positions are modelled by a two-dimensional diffusion equation. Compared to

17

1 Stangl et al.(*17*) where the path between two control points was approximated by a straight
2 line, we interpolated the trajectories by a piecewise linear approximation. Bold-faced letters
3 denote multi-dimensional vectors.

4 Let $\mathbf{x}$ be a path of length L parametrized by its length, i.e., $\mathbf{x}(0)$ and $\mathbf{x}(L)$ correspond to the
5 starting and the finishing point, respectively. Let $\hat{\mathbf{x}}(\ell)$ be the internal location estimate of the
6 participant's actual position $\mathbf{x}(\ell)$ for $0 \leq \ell \leq L$. The distance model from Stangl et al.(*17*)

$$7 \qquad \frac{\mathrm{d}\hat{\mathbf{x}}(\ell)}{\mathrm{d}\ell} = -\beta\hat{\mathbf{x}}(\ell) + \alpha\mathbf{v}(\ell) + \mathbf{b} + \sigma_0\boldsymbol{\xi}(\ell), \qquad (1)$$

8 where:

- 9 β is the location memory decay. If $\beta = 0$, the participant can incorporate the inputs on
10 the right-hand side of Eq. (1) into the estimate of $\hat{\mathbf{x}}(\ell)$ perfectly. If $\beta > 0$, the
11 participant will slowly forget the previous inputs. Models of this type are known as
12 "leaky integrators".

- 13 $\mathbf{v}(\ell) = \mathrm{d}\mathbf{x}(\ell)/\mathrm{d}\ell$ is the normalized velocity at $\mathbf{x}(\ell)$. Since the path is parametrized by
14 the distance, it follows that $|\mathbf{v}(\ell)| = 1$ for all $0 \leq \ell \leq L$.

- 15 α is the multiplicative velocity gain. The value $\alpha = 1$ corresponds to the correct
16 evaluation of the contribution of $\mathbf{v}$ on the location estimate. The cases $0 < \alpha < 1$ and
17 $1 < \alpha$ describe systematic underestimation and overestimation of the same effect,
18 respectively.

- 19 $\mathbf{b}$ is the additive bias, i.e., the direction in which the internal estimate is being
20 systematically shifted.

- 21 σ_0 is the accumulating noise (standard deviation). If $\sigma_0 = 0$, the internal location
22 estimate is not affected by the accumulating noise.

- 23 $\boldsymbol{\xi}$ is two-dimensional normally distributed Gaussian noise uncorrelated in ℓ. Formally,
24 the noise is a derivative of the two-dimensional Brownian motion.

25 We note that for $\beta = 0$, $\sigma_0 = 0$, $\alpha = 1$ and $\mathbf{b} = \mathbf{0}$, the estimate $\hat{\mathbf{x}}$ perfectly reflects the actual
26 position $\mathbf{x}$.

Segment reformulation

28 Assume that the path is split into K segments marked by stopping points $\mathbf{s}_k$, $k = 0,1,2,\dots,K$,
29 so that $\mathbf{s}_k = \mathbf{x}(\ell_k)$ for some $\ell_k \in [0, L]$ with $\ell_0 = 0$ and $\ell_K = L$. Let $\Delta\ell_k = \ell_k - \ell_{k-1}$, where
30 $k = 1,2,\dots,K$, be the length of the k-th segment of the path. The internal estimate $\hat{\mathbf{x}}_k$ at the
31 stopping point $\mathbf{s}_k$ can be recovered from the participant's report of distance estimate $\hat{d}$ and the
32 estimate of angle $\hat{\varphi}$ to the starting point $\mathbf{x}_{\text{start}}$ by

$$33 \qquad \hat{\mathbf{x}}_k = \begin{pmatrix} \hat{d}\cos(\hat{\varphi}) \\ \hat{d}\sin(\hat{\varphi}) \end{pmatrix} + \mathbf{x}_{\text{start}}. \qquad (2)$$

34 We set $\mathbf{x}_{\text{start}} = \mathbf{0}$. Given the internal estimate $\hat{\mathbf{x}}_k := \hat{\mathbf{x}}(\ell_k)$ of location at the stopping point $\mathbf{s}_k$,
35 the internal estimate of $\hat{\mathbf{x}}_{k+1}$ have a Gaussian distribution given by

$$36 \qquad \mathbb{P}(\hat{\mathbf{x}}_{k+1} \mid \hat{\mathbf{x}}_k; \theta) = \mathcal{N}(\hat{\mathbf{x}}_{k+1} \mid \boldsymbol{\mu}_{k+1}(\hat{\mathbf{x}}_k), \sigma_{k+1}^2\mathrm{Id}_2), \qquad (3)$$

1 where $\theta = (\beta, \alpha, \mathbf{b}, \sigma_0)$ are the model parameters, Id_2 is the two-dimensional identity matrix,
2 and the mean $\boldsymbol{\mu}_{k+1}$ and the variance σ^2_{k+1} are defined by

3
$$\boldsymbol{\mu}_{k+1}(\hat{\mathbf{x}}) = \hat{\mathbf{x}}e^{-\beta \Delta \ell_{k+1}} + \frac{\mathbf{b}}{\beta}\left(1 - e^{-\beta \Delta \ell_{k+1}}\right) + \alpha e^{-\beta \Delta \ell_{k+1}} \int_{\ell_k}^{\ell_{k+1}} e^{\beta(\ell - \ell_k)} \mathbf{v}(\ell)\, \mathrm{d}\ell, \qquad (4)$$

4 and

5
$$\sigma^2_{k+1} = \frac{\sigma_0^2}{2\beta}\left(1 - e^{-2\beta \Delta \ell_{k+1}}\right),$$

6 respectively (see supplemental material for complete derivation).

7 In Stangl et al.(*17*), the integral term in Eq. (4) is simplified by an additional assumption of a
8 constant velocity along each segment, effectively approximating the trajectory of each segment
9 by a straight line. In contrast, we have not imposed this additional assumption, which renders
10 the integral analytically unsolvable in general. For our purposes, it was sufficient to employ a
11 numerical method to approximate the integral with higher precision.

12 **Reporting noise**

13 We consider reporting noise as a normal distribution with zero mean and variance σ^2_{rep}
14 independent of $\boldsymbol{\xi}$, reflecting the spread of the responses around the internally estimated location
15 in Eq. (2). The reported internal location therefore satisfies:

16
$$\hat{\mathbf{x}}_{k+1} \mid \hat{\mathbf{x}}_k; \theta \sim \mathcal{N}(\boldsymbol{\mu}_{k+1}(\hat{\mathbf{x}}_k), \sigma^2_{k+1}\mathrm{Id}_2) + \mathcal{N}(\mathbf{0}, \sigma^2_{\mathrm{rep}}\mathrm{Id}_2).$$

17 Thanks to the independence of $\boldsymbol{\xi}$ and the reporting noise, the density of the reported internal
18 location simplifies to:

19
$$\mathbb{P}(\hat{\mathbf{x}}_{k+1} \mid \hat{\mathbf{x}}_k; \theta) = \mathcal{N}(\hat{\mathbf{x}}_{k+1} \mid \boldsymbol{\mu}_{k+1}(\hat{\mathbf{x}}_k), (\sigma^2_{k+1} + \sigma^2_{\mathrm{rep}})\mathrm{Id}_2).$$

20 Following Weber's law, we assume that the standard deviation of the reporting noise is
21 proportional to the participants' reported distance $\hat{d}_k$ (at the end of the k-th segment),
22 i.e. $\sigma_{\mathrm{rep}} = \sigma_r \hat{d}_k$:

23
$$\mathbb{P}(\hat{\mathbf{x}}_{k+1} \mid \hat{\mathbf{x}}_k; \theta) = \mathcal{N}(\hat{\mathbf{x}}_{k+1} \mid \boldsymbol{\mu}_{k+1}(\hat{\mathbf{x}}_k), (\sigma^2_{k+1} + \sigma_r^2 \hat{d}_k^2)\mathrm{Id}_2), \qquad (5)$$

24 where $\theta = (\beta, \alpha, \mathbf{b}, \sigma_0, \sigma_r)$ are the model parameters.

25 **Bayesian hierarchical model**
26 We employed a Bayesian approach(*73*), MCMC sampling, to estimate the posterior
27 distributions of the model parameters. The likelihood for a single path segment is given by
28 Eq. (5). Consequently, the likelihood function for the whole path is:
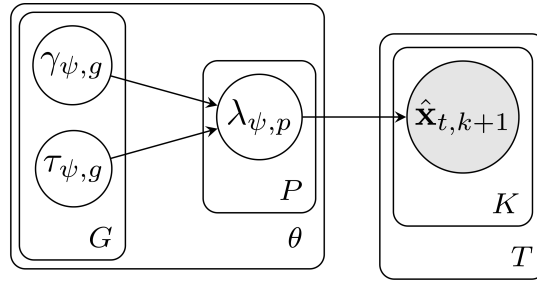
19

$$\mathcal{L}(\hat{\mathbf{x}}_K|\hat{\mathbf{x}}_{K-1}, \dots, \hat{\mathbf{x}}_0; \theta) = \prod_{k=0}^{K-1} \mathbb{P}(\hat{\mathbf{x}}_{k+1}|\hat{\mathbf{x}}_k; \theta).$$

For T trials, let $\hat{\mathbf{X}}_k = \left(\hat{\mathbf{x}}_k^{(1)}, \dots, \hat{\mathbf{x}}_k^{(T)}\right)$ denote the vector of T reports at the k-th control point. The overall likelihood function is then defined by:

$$\mathcal{L}(\hat{\mathbf{X}}_K|\hat{\mathbf{X}}_{K-1}, \dots, \hat{\mathbf{X}}_0; \theta) = \prod_{t=1}^{T} \mathcal{L}\left(\hat{\mathbf{x}}_K^{(t)}\Big|\hat{\mathbf{x}}_{K-1}^{(t)}, \dots, \hat{\mathbf{x}}_0^{(t)}; \theta\right).$$

If $\mathbb{P}(\theta)$ represents the prior distribution over the parameters, the posterior distribution is:

$$\mathbb{P}(\theta|\hat{\mathbf{X}}_K, \dots, \hat{\mathbf{X}}_0) \propto \mathcal{L}(\hat{\mathbf{X}}_K|\hat{\mathbf{X}}_{K-1}, \dots, \hat{\mathbf{X}}_0; \theta)\mathbb{P}(\theta). \tag{6}$$

Fig. 7. Graphical Representation of the Bayesian Hierarchical Model.
The group-level hyper-parameters $\gamma_{\psi,g}$ and $\tau_{\psi,g}$, associated with group plate G, govern the individual-level parameter $\lambda_{\psi,p}$, enclosed in the participant plate P. Each participant undergoes multiple trials, represented by the outer trial plate T, with each trial having multiple path segments captured by the inner plate K. The observed data $\hat{\mathbf{x}}_k^t$ at segment $k + 1$ in trial t is influenced by the parameter $\lambda_{\psi,p}$. Here ψ stands for any of five model parameters under parameter plate θ.

We introduced two levels of hierarchy into each model parameter ψ: individual and group level, represented using the plate notation (Fig. 7). At the individual level, parameters from participants within the same group are assumed to follow the same prior distribution governed by the group-level parameters. Specifically, for a given parameter ψ associated with the participant p from group g (either Control or SCD) has a distribution $\mathcal{D}$ with location $\gamma_{\psi,g}$ and scale $\tau_{\psi,g}$

$$\lambda_{\psi,p} \sim \mathcal{D}(\gamma_{\psi,g}, \tau_{\psi,g}).$$

For accumulating noise σ_0 and reporting noise σ_r, $\mathcal{D}$ is Gaussian$_+$. For all other parameters $\mathcal{D}$ is a Gaussian. The group-level hyper-parameters $\gamma_{\psi,g}$ and $\tau_{\psi,g}$ have their own respective priors $\mathcal{H}_1$ and $\mathcal{H}_2$:

$$\gamma_{\psi,g} \sim \mathcal{H}_1(\cdot), \quad \tau_{\psi,g} \sim \mathcal{H}_2(\cdot).$$

Details regarding the specific prior distribution of hyper-parameters, including their locations and scales, are provided in the supplemental material.

Since an analytical solution for the posterior distribution in Eq. (6) is not available, we used the No-U-Turn Sampler (NUTS) to generate posterior samples of the model parameters (*27*). The inference was conducted using NumPyro(*74*) with four independent MCMC chains, each run

20

1   for 1000 warm-up iterations followed by 1000 sampling iterations. To assess model
2   performance, we used leave-one-out expected log pointwise predictive density, $elpd_{loo}$.
3
4   **Statistics and reproducibility**
5   **PI and AI error analysis**
6   For statistical quantification, all analyses were conducted in R. To examine the relationship
7   between group status, stopping point, we used robust multiple linear regression with the MASS
8   package in RStudio, as the Shapiro-Wilk test indicated non-normal residuals ($p < 0.05$). These
9   models assessed associations of these factors with two primary outcomes: PI error (m) and AI
10   error (°). Covariates included 'sex', 'age', and 'MoCA', and due to evidence suggesting sex-
11   specific effects in AD pathology[75], a 'sex by group' interaction term was also added.
12
13   Continuous covariates were scaled and centred to normalize their range. We applied sum
14   contrasts for binary factors such as group (control vs. SCD) and sex (male vs. female), and
15   successive differences contrasts for stopping point, comparing intermediate versus final
16   stopping points.
17
18   **Blood and genetic biomarker analysis**
19   To evaluate whether PI performance and key computational model parameters were related to
20   biological and genetic markers of neuropathology (pTau 181, NFL and APOE status), we
21   modelled PI error and parameters such as the absolute deviation from optimal velocity gain (1),
22   beta, additive bias, accumulating noise, and reporting noise as dependent variables, influenced
23   by standardised (scaled and centred) plasma biomarker concentrations. All models included
24   age as a covariate. Given the violation of normality, robust regression from the MASS package
25   was employed to capture these relationships accurately. Sum contrasts were used for APOE
26   status (carriers and noncarriers).
27
28   To evaluate the unique contribution of plasma NFL levels to specific error sources, partial R^2
29   values were calculated. For each dependent variable (e.g., reporting noise, velocity gain), we
30   compared the variance explained by full regression models including NFL with reduced
31   models excluding NFL. Partial R^2 was computed as the proportion of variance uniquely
32   attributed to NFL, reflecting its specific predictive contribution to the model.
33
34   **Group comparisons on demographic variables, blood biomarkers and movement**
35   **characteristics**
36   For simple group differences, Bayesian t-tests were conducted. Where variances were equal,
37   we used ttestBF from the BayesFactor package in R; in cases of unequal variances, as in age,
38   and gait, we modelled variance separately for each group using the brm function from the brms
39   package. This method applied to demographic variables (age, MoCA, self-reported spatial
40   abilities, visuo-spatial working memory, gait and number of completed trials) as well as group
41   comparisons for blood biomarkers (pTau181, NFL) and movement metrics (head movements,
42   angular and translational velocity, and head pitch).
43
44   For comparisons between first 10% and last 10% of trials on changes in PI performance and
44   movement dynamics from early to late trials, we used linear regression analysis with sum
45   contrasts for both group and trial period (first 10% and last 10%).
46
47   **Modelling analysis**
47   *Individual-level* To examine differences for the individual (mean) level error sources, we used
48   robust linear regressions from the MASS package to account for violations of the normality
49   assumption in residuals. Separate models were fitted for each model parameter, with age

21

included as a covariate. The parameters analyzed included memory leak (β), velocity gain (α), additive bias ($||\mathbf{b}||$), accumulating noise (σ_0^2), and reporting noise (σ_r^2). Sum contrasts were used for group were used (Control/SCD).

Group-level For group-level analysis, we examined the posterior distributions of the model parameters to assess credible differences between groups. The analysis focused on the 95% Highest Density Interval (HDI), a key concept in Bayesian inference that indicates the range within which the most credible values of a parameter lie. Whether zero falls within this interval is crucial for interpreting the strength of evidence for an effect. If zero is excluded from the 95% HDI, it suggests statistically credible evidence of an effect, while inclusion of zero indicates the data do not rule out the possibility of no effect, reflecting uncertainty about the presence of a true difference. Additionally, we applied the Region of Practical Equivalence (ROPE)(*29*) to determine whether observed effects were practically negligible. The ROPE defines a range around the null value (often zero) within which differences are considered too small to be meaningful in practice. If most of the posterior distribution (e.g., 95% HDI) falls within the ROPE, the effect can be considered practically equivalent to the null value. We used ArviZ, NumPy, and Matplotlib to perform group-level analysis.

References

1. A. S. Etienne, K. J. Jeffery, Path integration in mammals. *Hippocampus* **14**, 180–192 (2004).

2. R. F. Wang, Building a cognitive map by assembling multiple path integration systems. *Psychon Bull Rev* **23**, 692–702 (2016).

3. M. Gil, M. Ancau, M. I. Schlesiger, A. Neitz, K. Allen, R. J. D. Marco, H. Monyer, Impaired path integration in mice with disrupted grid cell firing. *Nat Neurosci* **21**, 81–91 (2018).

4. H. Braak, E. Braak, Neuropathological stageing of Alzheimer-related changes. *Acta Neuropathol.* **82**, 239–259 (1991).

5. J. Ying, A. Reboreda, M. Yoshida, M. P. Brandon, Grid cell disruption in a mouse model of early Alzheimer's disease reflects reduced integration of self-motion cues. *Curr Biol* **33**, 2425-2437.e5 (2023).

6. H. Fu, G. A. Rodriguez, M. Herman, S. Emrani, E. Nahmani, G. Barrett, H. Y. Figueroa, E. Goldberg, S. A. Hussaini, K. E. Duff, Tau pathology induces excitatory neuron loss, grid cell dysfunction, and spatial memory deficits reminiscent of early alzheimer's disease. *Neuron* **93**, 533-541.e5 (2017).

7. A. Bierbrauer, L. Kunz, C. A. Gomes, M. Luhmann, L. Deuker, S. Getzmann, E. Wascher, P. D. Gajewski, J. G. Hengstler, M. Fernandez-Alvarez, M. Atienza, D. M. Cammisuli, F. Bonatti, C. Pruneti, A. Percesepe, Y. Bellaali, B. Hanseeuw, B. A. Strange, J. L. Cantero, N. Axmacher, Unmasking selective path integration deficits in Alzheimer's disease risk carriers. *Sci Adv* **6**, eaba1394 (2020).

8. I. Mokrisova, J. Laczo, R. Andel, I. Gazova, M. Vyhnalek, Z. Nedelska, D. Levcik, J. Cerman, K. Vlcek, J. Hort, Real-space path integration is impaired in Alzheimer's disease and mild cognitive impairment. *Behav Brain Res* **307**, 150–158 (2016).

9. D. Howett, A. Castegnaro, K. Krzywicka, J. Hagman, D. Marchment, R. Henson, M. Rio, J. A. King, N. Burgess, D. Chan, Differentiation of mild cognitive impairment using an entorhinal cortex-based test of virtual reality navigation. *Brain* **142**, 1751–1766 (2019).

10. L.-K. Huang, Y.-C. Kuan, H.-W. Lin, C.-J. Hu, Clinical trials of new drugs for Alzheimer disease: a 2020-2023 update. *J Biomed Sci* **30**, 83 (2023).

11. C. H. van Dyck, C. J. Swanson, P. Aisen, R. J. Bateman, C. Chen, M. Gee, M. Kanekiyo, D. Li, L. Reyderman, S. Cohen, L. Froelich, S. Katayama, M. Sabbagh, B. Vellas, D. Watson, S. Dhadda, M. Irizarry, L. D. Kramer, T. Iwatsubo, Lecanemab in early alzheimer's disease. *N Engl J Med* **388**, 9–21 (2023).

12. A. J. Mitchell, H. Beaumont, D. Ferguson, M. Yadegarfar, B. Stubbs, Risk of dementia and mild cognitive impairment in older people with subjective memory complaints: meta-analysis. *Acta Psychiatr Scand* **130**, 439–451 (2014).

13. F. Jessen, R. E. Amariglio, M. van Boxtel, M. Breteler, M. Ceccaldi, G. Chételat, B. Dubois, C. Dufouil, K. A. Ellis, W. M. van der Flier, L. Glodzik, A. C. van Harten, M. J. de Leon, P. McHugh, M. M. Mielke, J. L. Molinuevo, L. Mosconi, R. S. Osorio, A. Perrotin, R. C. Petersen, L. A. Rabin, L. Rami, B. Reisberg, D. M. Rentz, P. S. Sachdev, V. de la Sayette, A. J. Saykin, P. Scheltens, M. B. Shulman, M. J. Slavin, R. A. Sperling, R. Stewart, O. Uspenskaya, B. Vellas, P. J. Visser, M. Wagner, S. C. D. I. (SCD-I. W. Group, A conceptual framework for research on subjective cognitive decline in preclinical Alzheimer's disease. *Alzheimers Dement* **10**, 844–852 (2014).

14. R. F. Buckley, B. Hanseeuw, A. P. Schultz, P. Vannini, S. L. Aghjayan, M. J. Properzi, J. D. Jackson, E. C. Mormino, D. M. Rentz, R. A. Sperling, K. A. Johnson, R. E. Amariglio, Region-Specific Association of Subjective Cognitive Decline With Tauopathy Independent of Global β-Amyloid Burden. *JAMA Neurol* **74**, 1455–1463 (2017).

15. M. Lappe, M. Stiels, H. Frenz, J. M. Loomis, Keeping track of the distance from home by leaky integration along veering paths. *Exp Brain Res* **212**, 81–89 (2011).

16. M. Lappe, M. Jenkin, L. R. Harris, Travel distance estimation from visual motion by leaky path integration. *Exp Brain Res* **180**, 35–48 (2007).

17. M. Stangl, I. Kanitscheider, M. Riemer, I. Fiete, T. Wolbers, Sources of path integration error in young and aging humans. *Nat Commun* **11**, 2626 (2020).

18. J. T. Townsend, J. R. Busemeyer, J. K. Kruschke, W. Vanpaemel, "Bayesian estimation in hierarchical models" in *The Oxford Handbook of Computational and Mathematical Psychology*, ["Townsend, James T. and Busemeyer, Jerome R."], Eds. (Oxford University Press, 2015; http://www.oxfordhandbooks.com/view/10.1093/oxfordhb/9780199957996.001.0001/oxfordhb-9780199957996-e-13).

19. V. Segen, J. Ying, E. Morgan, M. Brandon, T. Wolbers, Path integration in normal aging and Alzheimer's disease. *Trends Cogn Sci (Regul Ed)* **26**, 142–158 (2022).

20. J. M. Wiener, A. Berthoz, T. Wolbers, Dissociable cognitive mechanisms underlying human path integration. *Exp Brain Res* **208**, 61–71 (2011).

21. E. K. Sadalla, D. R. Montello, Remembering changes in direction. *Environ Behav* **21**, 346–363 (1989).

22. A. Castegnaro, Z. Ji, K. Rudzka, D. Chan, N. Burgess, Overestimation in angular path integration precedes Alzheimer's dementia. *Curr Biol* **33**, 4650-4661.e7 (2023).

23. O. Mahmood, D. Adamo, E. Briceno, S. D. Moffat, Age differences in visual path integration. *Behav Brain Res* **205**, 88–95 (2009).

24. D. M. Wrisley, G. F. Marchetti, D. K. Kuharsky, S. L. Whitney, Reliability, internal consistency, and validity of data obtained with the functional gait assessment. *Phys Ther* **84**, 906–918 (2004).

25. C. J. Duffy, R. H. Wurtz, Response of monkey MST neurons to optic flow stimuli with shifted centers of motion. *J Neurosci* **15**, 5192–5208 (1995).

26. M. Lappe, F. Bremmer, van den Berg AV, Perception of self-motion from visual flow. *Trends Cogn Sci (Regul Ed)* **3**, 329–336 (1999).

27. M. D. Hoffman, A. Gelman, The No-U-Turn Sampler: Adaptively Setting Path Lengths in Hamiltonian Monte Carlo. *Journal of Machine Learning Research*, 1593–1623 (2014).

28. A. Vehtari, A. Gelman, J. Gabry, Practical Bayesian model evaluation using leave-one-out cross-validation and WAIC. *Stat Comput* **27**, 1413–1432 (2017).

29. J. K. Kruschke, Rejecting or Accepting Parameter Values in Bayesian Estimation. *Adv. Methods Pr. Psychol. Sci.* **1**, 270–280 (2018).

30. J. van Arendonk, F. J. Wolters, J. Neitzel, E. J. Vinke, M. W. Vernooij, M. Ghanbari, M. A. Ikram, Plasma neurofilament light chain in relation to 10-year change in cognition and neuroimaging markers: a population-based study. *Geroscience* **46**, 57–70 (2024).

31. S. Baiardi, C. Quadalti, A. Mammana, S. Dellavalle, C. Zenesini, L. Sambati, R. Pantieri, B. Polischi, L. Romano, M. Suffritti, G. M. Bentivenga, V. Randi, M. Stanzani-Maserati, S. Capellari, P. Parchi, Diagnostic value of plasma p-tau181, NfL, and GFAP in a clinical setting cohort of prevalent neurodegenerative dementias. *Alzheimers Res Ther* **14**, 153 (2022).

32. S. Janelidze, N. Mattsson, S. Palmqvist, R. Smith, T. G. Beach, G. E. Serrano, X. Chai, N. K. Proctor, U. Eichenlaub, H. Zetterberg, K. Blennow, E. M. Reiman, E. Stomrud, J. L. Dage, O. Hansson, Plasma P-tau181 in Alzheimer's disease: relationship to other biomarkers, differential diagnosis, neuropathology and longitudinal progression to Alzheimer's dementia. *Nat Med* **26**, 379–386 (2020).

33. E. H. Corder, A. M. Saunders, W. J. Strittmatter, D. E. Schmechel, P. C. Gaskell, G. W. Small, A. D. Roses, J. L. Haines, M. A. Pericak-Vance, Gene dose of apolipoprotein E type 4 allele and the risk of Alzheimer's disease in late onset families. *Science* **261**, 921–923 (1993).

34. D. E. Adamo, E. M. Briceño, J. A. Sindone, N. B. Alexander, S. D. Moffat, Age differences in virtual environment and real world path integration. *Front Aging Neurosci* **4**, 26 (2012).

35. G. L. Allen, K. C. Kirasic, M. A. Rashotte, D. B. M. Haun, Aging and path integration skill: kinesthetic and vestibular contributions to wayfinding. *Percept Psychophys* **66**, 170–179 (2004).

36. C. Newton, M. Pope, C. Rua, R. Henson, Z. Ji, N. Burgess, C. T. Rodgers, M. Stangl, M.-E. Dounavi, A. Castegnaro, I. Koychev, P. Malhotra, T. Wolbers, K. Ritchie, C. W. Ritchie, J. O'Brien, L. Su, D. Chan, P. D. R. Programme, Entorhinal-based path integration selectively predicts midlife risk of Alzheimer's disease. *Alzheimers Dement* **20**, 2779–2793 (2024).

37. A. Vandierendonck, E. Kemps, M. C. Fastame, A. Szmalec, Working memory components of the Corsi blocks task. *Br. J. Psychol.* **95**, 57–79 (2004).

38. T. Gómez-Isla, J. L. Price, D. W. McKeel, J. C. Morris, J. H. Growdon, B. T. Hyman, Profound loss of layer II entorhinal cortex neurons occurs in very mild Alzheimer's disease. *J Neurosci* **16**, 4491–4500 (1996).

39. L. Kunz, T. N. Schröder, H. Lee, C. Montag, B. Lachmann, R. Sariyska, M. Reuter, R. Stirnberg, T. Stöcker, P. C. Messing-Floeter, J. Fell, C. F. Doeller, N. Axmacher, Reduced grid-cell–like representations in adults at genetic risk for Alzheimer's disease. *Science* **350**, 430–433 (2015).

40. H. Jun, A. Bramian, S. Soma, T. Saito, T. C. Saido, K. M. Igarashi, Disrupted Place Cell Remapping and Impaired Grid Cells in a Knockin Model of Alzheimer's Disease. *Neuron* **107**, 1095-1112.e6 (2020).

41. J. Ying, A. T. Keinath, R. Lavoie, E. Vigneault, S. E. Mestikawy, M. P. Brandon, Disruption of the grid cell network in a mouse model of early Alzheimer's disease. *Nature Communications* **13**, 886 (2022).

42. Y. Burak, I. Fiete, Accurate path integration in continuous attractor network models of grid cells. *PLoS Comput Biol* **5** (2009).

43. L. Verret, E. O. Mann, G. B. Hang, A. M. I. Barth, I. Cobos, K. Ho, N. Devidze, E. Masliah, A. C. Kreitzer, I. Mody, L. Mucke, J. J. Palop, Inhibitory interneuron deficit links altered network activity and cognitive dysfunction in Alzheimer model. *Cell* **149**, 708–721 (2012).

44. H. Pastoll, L. Solanka, M. C. W. van Rossum, M. F. Nolan, Feedback Inhibition Enables Theta-Nested Gamma Oscillations and Grid Firing Fields. *Neuron* **77**, 141–154 (2013).

45. T. Rodríguez-Martín, A. M. Pooler, D. H. W. Lau, G. M. Mórotz, K. J. D. Vos, J. Gilley, M. P. Coleman, D. P. Hanger, Reduced number of axonal mitochondria and tau hypophosphorylation in mouse P301L tau knockin neurons. *Neurobiol Dis* **85**, 1–10 (2016).

46. L. L. Colgin, Mechanisms and functions of theta rhythms. *Annu Rev Neurosci* **36**, 295–312 (2013).

47. M. P. Brandon, A. R. Bogaard, C. P. libby, M. A. connerney, K. Gupta, M. E. Hasselmo, Reduction of theta rhythm dissociates grid cell spatial periodicity from directional tuning. *Science (New York, NY)* **332**, 595–599 (2011).

48. J. Koenig, A. N. Linder, J. K. Leutgeb, S. Leutgeb, The spatial periodicity of grid cells is not sustained during reduced theta oscillations. *Science (New York, NY)* **332**, 592–595 (2011).

49. J. J. Hernández-Pérez, K. W. Cooper, E. L. Newman, Medial entorhinal cortex activates in a traveling wave in the rat. *eLife* **9**, 493 (2020).

50. S. J. C. Venditto, B. Le, E. L. Newman, Place cell assemblies remain intact, despite reduced phase precession, after cholinergic disruption. *Hippocampus* **31**, 1065 (2019).

51. E. L. Newman, S. J. C. Venditto, J. R. Climer, E. A. Petter, S. N. Gillet, S. Levy, Precise spike timing dynamics of hippocampal place cell activity sensitive to cholinergic disruption. *Hippocampus* **27**, 1069–1082 (2017).

52. E. L. Newman, M. E. Hasselmo, Grid cell firing properties vary as a function of theta phase locking preferences in the rat medial entorhinal cortex. *Frontiers in systems neuroscience* **8**, 193 (2014).

53. T. Nakazono, T. N. Lam, A. Y. Patel, M. Kitazawa, T. Saito, T. C. Saido, K. M. Igarashi, Impaired In Vivo Gamma Oscillations in the Medial Entorhinal Cortex of Knock-in Alzheimer Model. *Front Syst Neurosci* **11**, 48 (2017).

54. J. J. Palop, L. Mucke, Network abnormalities and interneuron dysfunction in Alzheimer disease. *Nat Rev Neurosci* **17**, 777–792 (2016).

55. H. Hampel, M. M. Mesulam, A. C. Cuello, M. R. Farlow, E. Giacobini, G. T. Grossberg, A. S. Khachaturian, A. Vergallo, E. Cavedo, P. J. Snyder, Z. S. Khachaturian, The cholinergic system in the pathophysiology and treatment of Alzheimer's disease. *Brain : a journal of neurology* **141**, 1917–1933 (2018).

56. E. L. Newman, J. R. Climer, M. E. Hasselmo, Grid cell spatial tuning reduced following systemic muscarinic receptor blockade. *Hippocampus* **24**, 643–655 (2014).

57. E. L. Newman, S. N. Gillet, J. R. Climer, M. E. Hasselmo, Cholinergic Blockade Reduces Theta-Gamma Phase Amplitude Coupling and Speed Modulation of Theta Frequency Consistent with Behavioral Effects on Encoding. *The Journal of neuroscience : the official journal of the Society for Neuroscience* **33**, 19635–19646 (2013).

58. L. Colmant, A. Bierbrauer, Y. Bellaali, L. Kunz, J. V. Dongen, K. Sleegers, N. Axmacher, P. Lefèvre, B. Hanseeuw, Dissociating effects of aging and genetic risk of sporadic Alzheimer's disease on path integration. *Neurobiol Aging* **131**, 170–181 (2023).

59. S. S. Winter, B. J. Clark, J. S. Taube, Spatial navigation. Disruption of the head direction cell network impairs the parahippocampal grid cell signal. *Science* **347**, 870–874 (2015).

60. Y. Ma, L. Yu, M. Olah, R. Smith, S. R. Oatman, M. Allen, E. Pishva, B. Zhang, V. Menon, N. Ertekin-Taner, K. Lunnon, D. A. Bennett, H. Klein, P. L. D. Jager, Epigenomic features related to microglia are associated with attenuated effect of APOE ε4 on Alzheimer's disease risk in humans. *Alzheimer's Dement.* **18**, 688–699 (2021).

61. E. Angelopoulou, Y. N. Paudel, S. G. Papageorgiou, C. Piperi, APOE Genotype and Alzheimer's Disease: The Influence of Lifestyle and Environmental Factors. *ACS Chem. Neurosci.* **12**, 2749–2764 (2021).

62. J. D. Marks, J. A. Syrjanen, J. Graff-Radford, R. C. Petersen, M. M. Machulda, M. R. Campbell, A. Algeciras-Schimnich, V. Lowe, D. S. Knopman, C. R. Jack, P. Vemuri, M. M. Mielke, A. D. N. Initiative, Comparison of plasma neurofilament light and total tau as neurodegeneration markers: associations with cognitive and neuroimaging outcomes. *Alzheimers Res Ther* **13**, 199 (2021).

63. J. Arranz, N. Zhu, S. Rubio-Guerra, Í. Rodríguez-Baz, R. Ferrer, M. Carmona-Iragui, I. Barroeta, I. Illán-Gala, M. Santos-Santos, J. Fortea, A. Lleó, M. Tondo, D. Alcolea, Diagnostic performance of plasma pTau217, pTau181, Aβ1-42 and Aβ1-40 in the LUMIPULSE automated platform for the detection of Alzheimer disease. *Alzheimers Res Ther* **16**, 139 (2024).

64. E. E. Moore, T. J. Hohman, F. S. Badami, K. R. Pechman, K. E. Osborn, L. M. Y. Acosta, S. P. Bell, M. A. Babicz, K. A. Gifford, A. W. Anderson, L. E. Goldstein, K. Blennow, H. Zetterberg, A. L. Jefferson, Neurofilament relates to white matter microstructure in older adults. *Neurobiol Aging* **70**, 233–241 (2018).

65. S. Bells, J. Lefebvre, S. A. Prescott, C. Dockstader, E. Bouffet, J. Skocic, S. Laughlin, D. J. Mabbott, Changes in white matter microstructure impact cognition by disrupting the ability of neural assemblies to synchronize. *J Neurosci* **37**, 8227–8238 (2017).

66. A. M. Fjell, L. T. Westlye, I. K. Amlien, K. B. Walhovd, Reduced white matter integrity is related to cognitive instability. *J Neurosci* **31**, 18060–18072 (2011).

67. H. Maalmi, A. Strom, A. Petrera, S. M. Hauck, K. Strassburger, O. Kuss, O.-P. Zaharia, G. J. Bönhof, W. Rathmann, S. Trenkamp, V. Burkart, J. Szendroedi, D. Ziegler, M. Roden, C. Herder, G. Group, Serum neurofilament light chain: a novel biomarker for early diabetic sensorimotor polyneuropathy. *Diabetologia* **66**, 579–589 (2023).

68. N. S. Schmid, M. M. Ehrensperger, M. Berres, I. R. Beck, A. U. Monsch, The Extension of the German CERAD Neuropsychological Assessment Battery with Tests Assessing Subcortical, Executive and Frontal Functions Improves Accuracy in Dementia Diagnosis. *Dement. Geriatr. Cogn. Disord. Extra* **4**, 322–34 (2014).

69. Z. S. Nasreddine, N. A. Phillips, V. Bédirian, S. Charbonneau, V. Whitehead, I. Collin, J. L. Cummings, H. Chertkow, The Montreal Cognitive Assessment, MoCA: A brief screening tool for mild cognitive impairment. *J Am Geriatr Soc* **53**, 695–699 (2005).

70. N. Carson, L. Leach, K. J. Murphy, A re-examination of Montreal Cognitive Assessment (MoCA) cutoff scores. *Int J Geriatr Psychiatry* **33**, 379–388 (2018).

71. G. Stoet, PsyToolkit: A software package for programming psychological experiments using Linux. *Behav. Res. Methods* **42**, 1096–1104 (2010).

72. M.-F. Xiao, D. Xu, M. T. Craig, K. A. Pelkey, C.-C. Chien, Y. Shi, J. Zhang, S. Resnick, O. Pletnikova, D. Salmon, J. Brewer, S. Edland, J. Wegiel, B. Tycko, A. Savonenko, R. H.

1   Reeves, J. C. Troncoso, C. J. McBain, D. Galasko, P. F. Worley, NPTX2 and cognitive
2   dysfunction in Alzheimer's Disease. *eLife* **6** (2017).

3   73. A. Gelman, J. B. Carlin, H. S. Stern, D. B. Dunson, A. Vehtari, D. B. Rubin, *Bayesian*
4   *Data Analysis, Third Edition* (Chapman and Hall/CRC, 2013;
5   https://www.taylorfrancis.com/books/9781439898208).

6   74. D. Phan, N. Pradhan, M. Jankowiak, Composable Effects for Flexible and Accelerated
7   Probabilistic Programming in NumPyro. *arXiv*, doi: 10.48550/arxiv.1912.11554 (2019).

8   75. M. T. Ferretti, M. F. Iulita, E. Cavedo, P. A. Chiesa, A. S. Dimech, A. S. Chadha, F.
9   Baracchi, H. Girouard, S. Misoch, E. Giacobini, H. Depypere, H. Hampel, W. B. P. and the A.
10   P. M. Initiative, Sex differences in Alzheimer disease - the gateway to precision medicine. *Nat*
11   *Rev Neurol* **14**, 457–469 (2018).

12   **Acknowledgements**

22   **Author contributions:**
23   Conceptualization: VS, TW, EN, ZT, MKR
24   Methodology: VS, TW, ZT, AS, JS, MKR, WG, MB
25   Investigation: VS, MKR
26   Visualization: VS, MKR
27   Supervision: TW, ZT
28   Writing—original draft: VS, TW
29   Writing—review & editing: VS, TW, EN, ZT, AS, JS, MKR**,** WG, MB
30   **Competing interests:** The authors declare that they have no competing interests
31   **Data and material availability:** The summary and raw data used for the analyses, including
32   results from the computational modeling, are available on Figshare
33   (https://doi.org/10.6084/m9.figshare.28304303). Due to data privacy regulations, raw
34   individual positional data are not currently shared on Figshare but can be made available upon
35   reasonable request, subject to a data-sharing agreement**.** Code used for the computational
36   modelling is available on GitHub (https://github.com/cogneuroai/Bayesian-hierarchical-model-
37   for-PI). Code used to generated plots presented in this manuscript is available on OSF
38   (https://osf.io/fvw57)